

Fouzia Fahrin¹*, Alex O. Gonzalez^{1,2}, Brett Chrisler³, and Justin P. Stachnik³¹ Iowa State University, ² Woods Hole Oceanographic Institution, ³ University of Kansas

Modified from a manuscript published in Journal of Climate

1. INTRODUCTION

Tropical precipitation plays a significant role in global climate with surplus latent heating and redistributing energy in the Earth system, as well as a major source of uncertainties due to climate changes (Duffy et al. 2020, and the references therein). Most of the tropical precipitations happen within the rising branch of the Hadley cell, called the intertropical convergence zone (ITCZ). These precipitations are not sporadic but can get organized into different spatial scales ranging from mesoscale to planetary and are frequently modulated by zonally propagating convectively coupled waves (CCWs) (Wheeler et al. 2000; Kiladis et al. 2009). We use the term “CCW” here, which encompasses convectively coupled Kelvin, equatorial Rossby (ER), mixed Rossby-gravity (MRG), $n = 0$ eastward inertia-gravity (IG0), and $n = 1$ inertia-gravity (IG1) waves (Blandford 1966; Matsuno 1966) as well as tropical depression type disturbances (TD type, Takayabu and Nitta 1993) and the Madden-Julian oscillation (MJO, Madden and Julian 1971, 1972).

Due to the multi-scale nature of CCWs and their strong convective coupling, they continue to be severely misrepresented in Earth System Models (ESMs) (Hung et al. 2013; Guo et al. 2015; Judt and Rios-Berrios 2021). Studies showed that high-frequency CCWs (i.e., Kelvin, MRG, IG0, and IG1 waves) are generally too weak and low-frequency CCWs (i.e., ER waves and the MJO) are too strong in earth system models (Hung et al. 2013; Guo et al. 2015). This is often referred to as an over-reddened at all scales, included in the power spectrum (Lin et al. 2006).

At the same time, ESMs have long suffered from tropical precipitation biases in the ITCZ, often referred to as “double ITCZ” biases, especially in the East Pacific (EP) Ocean basin during boreal spring (February, March, and April, FMA) when the cold

tongues are weakest (Mechoso et al. 1995; Lin 2007; Wang et al. 2015; Zhang et al. 2015; Adam et al. 2016; Si et al. 2021). During FMA, the EP ITCZ recedes southward to its most equatorward position with relatively shallow convection (Huaman and Takahashi 2016), and often, a second ITCZ appears in the SH (Fig. 1). The presence of one ITCZ in each hemisphere is often referred to as a double ITCZ (Hubert et al. 1969; Zhang 2001; Gu et al. 2005). However, a double ITCZ does not occur consistently during FMA due to large sub-seasonal variability in ITCZ position (Henke et al. 2012; Haffke et al. 2016; Gonzalez et al. 2022) and strong interannual variability due to El Niño Southern Oscillation (ENSO, Yang and Magnusdottir 2016). Due to the highly variable ITCZ behavior in the EP during FMA, many models with double ITCZ biases produce too much precipitation in the Southern Hemisphere (SH) and not enough precipitation in the Northern Hemisphere (NH) in the EP during FMA (Wang et al. 2015; Song and Zhang 2019; Si et al. 2021).

In this study, we aim to analyze the interaction between tropical precipitation and CCWs during FMA. We hypothesize that CCWs explain a significantly higher percentage of the variance in SH convection over the EP, especially during boreal spring. In order to link CCWs to the ITCZ more directly, we develop a new, precipitation-based ITCZ identification algorithm on daily timescales that complements similar data sets created by Henke et al. (2012) and Haffke et al. (2016). We expect that certain configurations of the ITCZ, e.g., when precipitation is amplified south of the equator in the EP, are largely due to CCWs propagating into the region from South America or the west-central Pacific Ocean (Mapes et al. 2003; Mayta et al. 2021).

2. DATA AND METHODS

2.1. Observational and Reanalysis Data Sets

Bilinear interpolated $1.0^\circ \times 1.0^\circ$ daily accumulated precipitation rates were obtained from NASA’s Integrated Multi-satellitE Retrievals for GPM (IMERG)

* Corresponding author address: Fouzia Fahrin, Department of Geological and Atmospheric Science, Iowa State University, Ames, IA 50011-3212; E-mail: fahrin@iastate.edu.

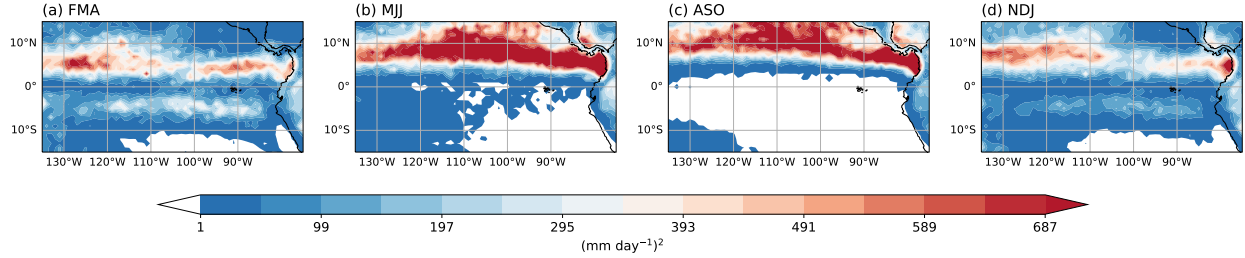


FIG. 1. Daily IMERG deseasonalized precipitation variance at three months intervals (2001–2021) from 75°W to 135°W. Variance less than $3 \text{ (mm day}^{-1}\text{)}^2$ are omitted.

for the years 2001–2021 (Huffman et al. 2015). For atmospheric dynamics fields such as geopotential heights, streamfunctions, and zonal and meridional wind, we used daily averaged 1.0° grid spaced data from the European Centre for Medium-range Weather Forecasts (ECMWF) ERA5 reanalysis for 2001–2021 (Hersbach et al. 2020).

2.2. Wave Type Filtering for CCWs

We employ space-time spectral analysis on the IMERG daily precipitation anomalies following the general methods in Wheeler and Kiladis (1999). Regional ($50^\circ\text{--}170^\circ\text{W}$) spectra are produced by applying a Hann window that tapers the IMERG data using a cosine weighting from a maximum at the domain center (i.e., 110°W) to zero at the edges of the domain as done in Dias and Kiladis (2014). Furthermore, raw January through April (JFMA) spectra are produced one year at a time and then averaged over all years during the 2001 to 2021 time frame.

For each JFMA season (120 or 121 days total), three 80-day spectra are produced with 60-day successively overlapping segments for a total of three segments per season (i.e., days 1-80, 21-100, and 41-120). Unlike in Wheeler and Kiladis (1999), we do not divide by a smoothed background spectrum to identify statistically significant spectral peaks. This is done in part to reduce information loss, such as slow-moving Kelvin waves, that may occur when removing a smoothed background (e.g., Roundy 2020). Figure 2 shows the 10°S to 10°N average of the \log_{10} of the symmetric and anti-symmetric raw power spectra for JFMA 2001–2021 over the EP ($50^\circ\text{--}170^\circ\text{W}$). It should be noted signals in low wavenumbers must be viewed with caution as we cannot fully resolve zonal wavenumber 3 or smaller due to our limited $50^\circ\text{--}170^\circ\text{W}$ domain.

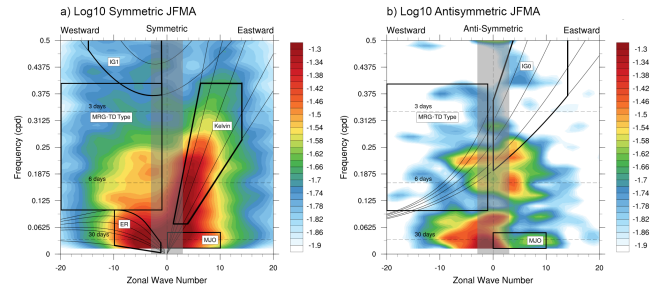


FIG. 2. Wavenumber-frequency power spectrum of the (a) symmetric and (b) anti-symmetric components of IMERG precipitation anomalies for January through April 2001–2021 over the EP ($10^\circ\text{S--}10^\circ\text{N}$, $50^\circ\text{--}170^\circ\text{W}$). The dispersion curves for Kelvin, MRG, and IG0 waves are plotted for equivalent depths of 8, 12, 25, 50, and 90 m. For the ER wave, the dispersion curves are for equivalent depths 1, 8, 12, 25, 50, and 90 m. Lastly, for IG1, the curves are for depths 12 and 25 m. Heavy solid boxes indicate the wavenumber vs. frequency filtering for each CCW used in this study (see Table 1). Gray shading indicates wavenumbers that are not fully resolved, given the longitudinal trimming applied to calculate the regional power spectrum.

2.3. Variance Calculation

The percent variance of total precipitation associated with each CCW filter wave band at a given point has been calculated to understand the CCW's influence on total precipitation. The variance calculation technique has been adopted from Schreck et al. (2013). The IMERG anomalies, already having their first four harmonics removed, are divided by their standard deviation (σ) at each grid point. The standardized anomalies are further filtered for the wavenumbers, frequencies, and equivalent depths associated with each wave type filter-

wave	wavenumber	period	depth
Kelvin	1 to 14	2.5 to 14 days	8 to 90 m
IG0	0 to 14	0.5 to 5.3 days	8 to 90 m
MRG-TD type	-20 to -1	2.5 to 10 days	none
ER	-10 to -1	10 to 96 days	1 to 90 m
MJO	0 to 10	20 to 70 days	none
IG1	-15 to -1	0.5 to 3 days	12 to 50 m

TABLE 1. Spectral window and equivalent depth used to filter CCWs.

ing domain as described in Table 1. The variance with respect to the time dimension of the filtered data classifies as the fraction of the total precipitation variance associated with each wave type filter band at each grid point. We must be careful while interpreting these values as they technically represent the fraction of the total variance that falls within a given wave filter domain and not simply the fraction of the total variance associated with a given wave type.

2.4. Lagged Regression and Estimates of Wave Properties

In order to produce the composite dynamical structure corresponding to the CCW-filtered precipitation, we applied lagged linear regression techniques from Wheeler et al. (2000) and Kiladis et al. (2009). We correlate and regress the space-time filtered anomalies of precipitation, horizontal winds, and either geopotential or streamfunction of a particular CCW band against its space-time filtered precipitation anomalies at a subjectively chosen base point in each hemisphere where a significant amount of variance for the filtered CCW is present. The base points are 5°N, 105°W and 5°S, 105°W in the NH and SH, respectively.

2.5. Daily East Pacific ITCZ states

The latitudinal location of the ITCZ, or ITCZ state, over the EP Ocean region (20°S–20°N, 90°–135°W) is determined from daily IMERG precipitation. We adopt the same ITCZ states as in Haf-

pr_{NH}	pr_{EQ}	pr_{SH}	ITCZ state
Strong	Weak	Weak	nITCZ
Strong	Strong	Weak	nITCZ
Weak	Weak	Strong	sITCZ
Weak	Strong	Strong	sITCZ
Strong	Weak	Strong	dITCZ
Weak	Weak	Weak	aITCZ
Weak	Strong	Weak	eITCZ
Strong	Strong	Strong	eITCZ

TABLE 2. ITCZ state decision table based on three precipitation metrics: i) NH precipitation (pr_{NH} , 2°N–20°N), ii) equatorial precipitation (pr_{EQ} , 1°S–1°N), and iii) SH precipitation (pr_{SH} , 2°S–20°S).

fke et al. (2016): double ITCZ (dITCZ), NH ITCZ (nITCZ), SH ITCZ (sITCZ), absent ITCZ (aITCZ), and equatorial ITCZ (eITCZ). In a similar vein as Hwang and Frierson (2013) and Adam et al. (2016), we compute three latitudinally averaged precipitation metrics: i) NH precipitation (pr_{NH}), ii) equatorial precipitation (pr_{EQ}), and iii) SH precipitation (pr_{SH}). Each of the three metrics is normalized by the 60th percentile of the 90°–135°W-averaged precipitation for that particular day. We determine whether each precipitation metric is “strong” or “weak” based on whether or not it is greater than or equal to 1. Table 2 shows the eight possible combinations of strong and weak designations for our three precipitation metrics. Figure 3 shows the spatial pattern of the ITCZ states from our new IMERG precipitation-based algorithm. We note that eITCZs occur only for some years, possibly associated with whether an equatorial cold tongue is present and the strength or flavor of ENSO (Yang and Magnusdottir 2016).

3. RESULTS

3.1. Seasonal Variability of CCWs over the East Pacific Ocean

Given that the deseasonalized precipitation variance is always smaller in the SH than in the NH (Fig. 1), we focus on investigating the impact of CCW variance associated with any given filtered wave band during the FMA season when the largest SH precipitation variance occurs. Before exclusively concentrating on the FMA season, we determine the season when most, if not all, filtered CCWs that fall within the frequency-wavenumber range defined by the filter band of the respective

IMERG Precipitation Rate (mm day⁻¹) daily ITCZ states (Feb-Apr, 2001-2021)

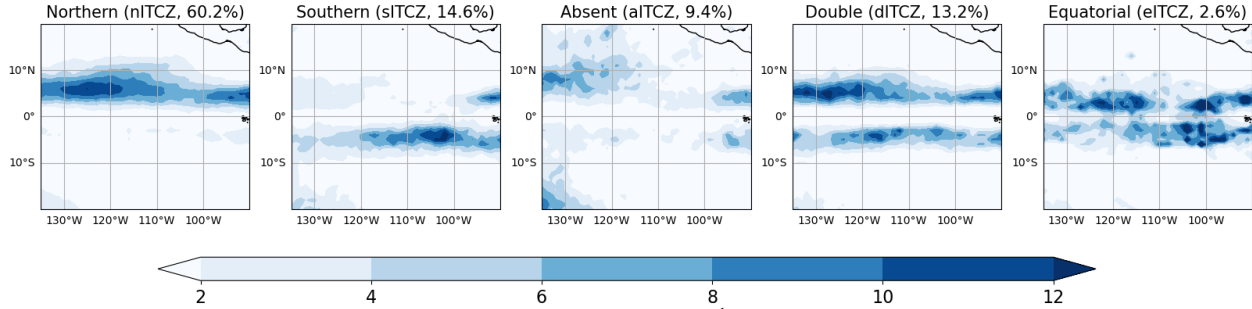


FIG. 3. FMA average IMERG precipitation rate (mm day⁻¹) composited for each daily EP ITCZ state: Northern (nITCZ), Southern (sITCZ), Absent (aITCZ), Double (dITCZ), and Equatorial (eITCZ) using the IMERG precipitation-based algorithm (2001–2021).

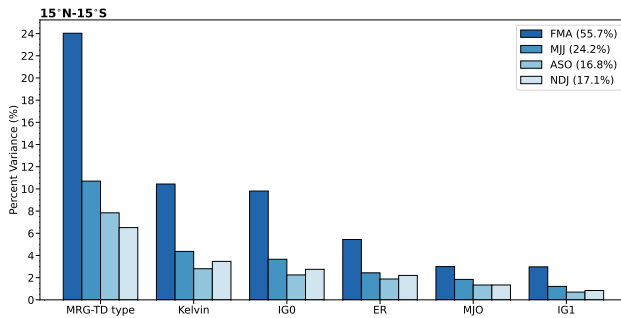


FIG. 4. Percent of total precipitation variance explained by the indicated filter bands of each wave type over the EP (75°–135°W) from 2001 to 2021 averaged between 15°N–15°S during FMA, MJJ, ASO, and NDJ.

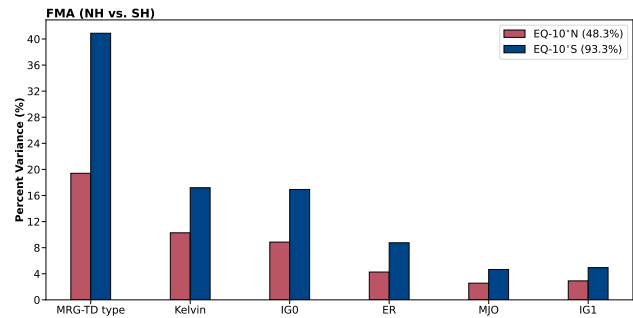


FIG. 5. Percent of total precipitation variance explained by each wave filter band over the EP (75°–135°W) from 2001 to 2021 averaged between EQ - 10°N and EQ - 10°S and for FMA denoted by the red and blue bars, respectively.

waves have the largest impact on the total precipitation variance through the percent or fractional variance (Schreck et al. 2013).

Figure 4 shows the seasonal variation for the percent variance of each CCW filter band spatially averaged over 15°S–15°N and 75°–135°W. The seasonal cycles of all the waves are relatively similar in the EP in that they explain the most variance during FMA (55.7%) and the least during November–January (NDJ, 17.1%) or August–October (ASO, 16.8%) (Fig. 4).

Figure 5 involves NH vs. SH spatial averaging of the FMA CCW filtered band percent variance over our focused EP region (75°–135°W). In Figure 5, the tropics have been divided into a NH (EQ–10°N) and SH (EQ–10°S) region over the EP. Precipitation variability in the SH is dominated by CCWs, resulting in 93.3% of the total variance. This supports the notion that the waves are far more active in the SH than the NH during FMA. However, as mentioned in section 2.3, these fractional variances

are overestimates of the true variance, and the variances explained by each wave filter band strongly depend on each filter box’s size and location. For example, boxes of equal frequency intervals will automatically have more variance at lower frequencies and wavenumbers due to the “redness” of the background spectrum in each wave domain.

3.2. Spatial and Temporal Variability of Kelvin Wave

In this section, we analyze the FMA time-lagged composite of precipitation and lower tropospheric dynamical fields of the Kelvin wave in both hemispheres. We note that the fraction variance calculation cautions in the last section apply much less to the regression approach used here since the assumption is that the background, although red, is truly random and should have minimal impact on the “signal” associated with the spectral peaks. The motivation for further inspecting Kelvin wave

is that Kelvin wave is one of the high-frequency CCWs highlighted as underestimated in earth system models (Guo et al. 2015). In the original manuscript, the spatial and temporal variability of IG0 and MRG-TD type are also analyzed. We only document Kelvin wave here to keep the paper length shorter.

Figure 6 shows the regressed precipitation anomalies, associated 850 hPa wind and geopotential height at the NH (5°N, 105°W) and SH base point (5°S, 105°W). Two days before the peak in convection, the positive precipitation anomaly signal is centered at about 130°W, and the precipitation and dynamical signals move eastward in subsequent lags at a phase velocity of approximately 17–18 m s⁻¹, and a period of approximately four days (0.25 cycles per day). In both hemispheres, the waves have an estimated zonal wavenumber of 6–7, consistent with the strong power shown in Figure 2. The wave-filtered precipitation and the dynamical fields for lag regression at our chosen base point are 95% significant. The statistical significance has been calculated at the $\alpha = 0.05$ level and is assessed at each grid point by using the field significance test of Wilks (2016).

The shape of the Kelvin wave convection is more zonally elongated and narrower in the EP compared to the warm pool (see Straub and Kiladis 2002, 2003; Kiladis et al. 2009). As anticipated based on equatorial wave theory (Matsuno 1966; Gill 1980), the horizontal winds at 850 hPa are mostly zonal at each of the three lags in both hemispheres. On a broad scale, the lower tropospheric height and wind pattern have an in-phase relationship and are nearly symmetric about the equator, similar to the theory (Kiladis et al. 2009). Heights are low with easterlies east of the maximum precipitation and high height with westerlies west of it as predicted by the shallow water (SW) theory (see Figure 3f of Kiladis et al. 2009), even though the stronger convective portion of the wave is significantly asymmetric about the equator. This pattern of near symmetry of the dynamical fields about the equator associated with off-equatorial strong convective signal is also seen in March–May (Huaman et al. 2020) and in June–August (Straub and Kiladis 2002, 2003). The meridional wind component becomes relatively large, close to the maximum positive precipitation anomalies.

At the SH base point (5°S, 105°W) in Fig. 6d–f, while there is enhanced precipitation near the

southern base point, the anomalous precipitation pattern is more symmetric about the equator than it is for the regressions at the NH base point (Fig. 6a–c). This precipitation pattern resembles more of a double ITCZ structure deviating from the theoretical SW mode (Matsuno 1966; Kiladis et al. 2009). The relatively strong precipitation signal in the NH seen in Fig. 6d–f may be due to the warm background SST to the north of the equator (Straub and Kiladis 2002).

3.3. CCW Variability as a Function of ITCZ States

To further analyze the relative CCW influence on the ITCZ over the EP during boreal spring, we examine how the CCW-filtered percent precipitation variance differs for each ITCZ state. To do this, we repeat the process of calculating the percent variance for each filtered CCW over the EP (10°S–10°N, 75°–135°W) but limit the composites to the subset of each ITCZ state days during FMA season.

The cumulative impact of filtered CCWs on precipitation variance for each ITCZ state (Figure 7) shows that the CCW contribution to the precipitation gradually increases from nITCZ (55.3%) to dITCZ (79.3%) with additional variance explained for sITCZ (105.9%) and eITCZ (121.5%) states. It is important to note that these fractional variances are overestimates of the true variance and are strongly dependent on the size and location of each filter box. The values higher than 100% represent a greater degree of variability, which occurs when the standard deviation exceeds the mean value of the dataset. The most dominant influence of CCWs on the precipitation variance occurs during sITCZ and eITCZ days. On the other hand, the nITCZ state is the most dominant state throughout the year, but CCW-filtered precipitation activity has a relatively small contribution to the total precipitation variability (Figure 7) when only the northern branch of ITCZ is active.

3.4. Co-evolution between ITCZ States and Leading High Frequency CCWs

Finally, we examine the co-evolution between ITCZ states and the three leading high-frequency CCWs (Kelvin, IG0, MRG-TD type) to determine if there is a significant lead-lag relationship. We analyze only strongly precipitating CCW days, which

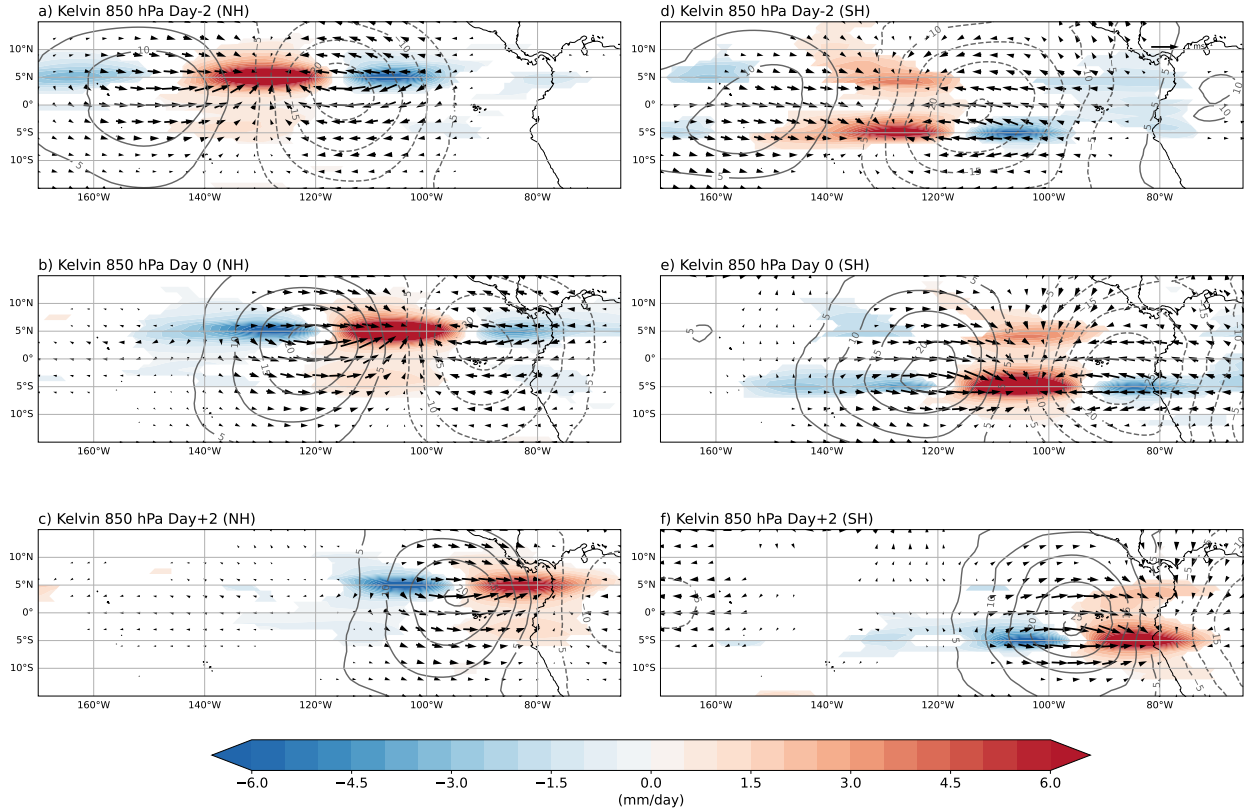


FIG. 6. Maps of Kelvin wave band filtered precipitation (shading), geopotential height (contours) and wind (vectors) anomalies associated with the Kelvin wave band filtered precipitation at the base point 5°N , 105°W , for day -2 , day 0 , and day $+2$ for (a)–(c) 850 hPa, and (d)–(f) 200 hPa. Geopotential height contours start at ± 25 m and the interval is 5 m with negative contours dashed. Shading and contours indicate regions significant at the 95% level. Wind vectors are plotted only where either the u or v component is significant at the 95% level or greater, with the largest wind vector as shown in the top-right corner. Every third vector is shown for readability.

are defined as the subset of FMA days when CCW precipitation anomalies exceed 1.0 standard deviation at the base point (NH or SH). These strong CCW days are averaged in time and considered as lag 0 for each respective CCW. We then quantify the time lag, from -15 to $+15$ days, as a function of longitude by computing the latitudinal average of the precipitation anomalies over $2.5^{\circ}\text{N} - 7.5^{\circ}\text{N}$ (NH) and $2.5^{\circ}\text{S} - 7.5^{\circ}\text{S}$ (SH).

To relate the leading high-frequency CCW precipitation activity with the ITCZ state, we start by calculating the ITCZ state percentage for strong wave activity days for lag -15 to $+15$, where lag 0 for each CCW type is the same as described above. The ITCZ state percentage is plotted as anomalies that are relative to the FMA percentages in Figure 3 after applying a five-day running mean to the percent-

age anomalies. To keep the paper length shorter, only the correlation between Kelvin wave and ITCZ is discussed here; we refer readers to the original paper for details.

Kelvin waves initiate in the central–west Pacific near day -5 and propagate into the EP (Figures 8a and 8c) and the precipitation signals in the SH are much weaker than in the NH, which is expected based on climatological precipitation variances for each CCW (not shown). The pattern of strong Kelvin wave variances over the entire Pacific basin agrees with past studies (Straub and Kiladis 2002; Roundy and Frank 2004).

In regards to the time evolution of ITCZ states for NH CCWs, there is a broadly increasing trend for nITCZs (black curves) and a decreasing trend for sITCZs (gold curves) while dITCZs (blue curves)

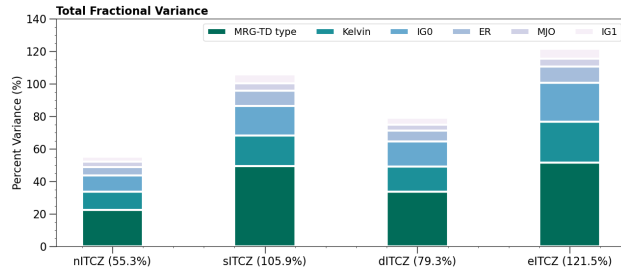


FIG. 7. Total variance of wave-filtered precipitation expressed as a fraction of the ITCZ states variance for all CCW bands. The variance has been calculated from 2001 through 2021 and averaged between (10°N – 10°S) and (75° – 135°W). We withhold aITCZ variances since there is less precipitation activity associated with this state.

decrease after lag 0 (Figure 8b). Together, the sITCZ and dITCZ trend (sITCZ+dITCZ, red curves) is strongly anticorrelated with nITCZs. The increasing frequency of the nITCZ state, particularly after lag 0, suggests that NH CCWs may act as a precursor and aid in the development of the nITCZ state.

For SH CCWs (Figure 8d, the ITCZ state percent anomalies are nearly double the NH CCWs ITCZ state percent anomalies (note the different abscissa). The sITCZs have the largest percentage increase, and nITCZ has the largest percentage decrease, both reaching their largest deviations near lag 0. The dITCZs show relatively smaller percent anomalies but have a somewhat more identifiable temporal peak near lag 0 than sITCZs. Similar to that of NH CCWs, the sITCZ+dITCZ trend is highly anti-correlated with the nITCZ trend. These results imply that SH CCWs can both aid in the development of sITCZs or dITCZs (i.e., positive ITCZ anomalies at positive lags) and be excited/amplified by sITCZs or dITCZs (i.e., increasing ITCZ state trends at negative lags that proceed CCWs).

4. SUMMARY AND CONCLUSION

In this study, we demonstrated that there is a significant impact of filtered CCWs on precipitation variability over the EP during boreal spring, the only season with significant precipitation activity in the SH, using IMERG precipitation and ERA5 reanalysis data. We employed commonly-used space-time filtering techniques (Wheeler and Kiladis 1999; Dias and Kiladis 2014, and many others). We computed the percent precipitation variance contributed by

each of six CCW band filtered precipitation (Kelvin, IG0, MRG-TD type, ER, MJO, and IG1) following the methods of Schreck et al. (2013) with respect to: i) all FMA days and ii) days associated with each of five different ITCZ configurations or “ITCZ states” (nITCZ, sITCZ, aITCZ, dITCZ, and eITCZ) based on our new daily precipitation-based ITCZ states algorithm.

The results show that the percent of CCW-filtered precipitation variances have a synchronized seasonal cycle of maximum variance explained during FMA and minimum variance explained during ASO or NDJ over the EP. Furthermore, the impact is more predominant with higher precipitation variance explained by filtered CCWs bands in the SH than in the NH. Caution must be taken comparing percentages between wave bands as the background variance inflates larger spectral widths, especially for the wide spectral band of MRG–TD type.

The composite time-evolving dynamical patterns of Kelvin wave during FMA at both base points broadly resemble the theoretically predicted modes from equatorial wave theory (Blandford 1966; Matsuno 1966; Wheeler et al. 2000; Kiladis et al. 2009). In contrast to the Indo-Pacific warm pool, we find a meridionally narrow and zonally elongated Kelvin wave precipitation band along with a weak but significant amount of lower tropospheric meridional wind component close to the maximum precipitation. At the NH base point, the Kelvin wave precipitation is north of the equator; however, in the SH, the precipitation anomalies are more like a double ITCZ pattern (Figure 6). This precipitation pattern in both hemispheres suggests that the anomalies follow the boreal spring background SST pattern (Straub and Kiladis 2002; Kiladis et al. 2009).

Our analysis suggests that the filtered CCW bands have a stronger impact on the EP ITCZ when precipitation occurs in the SH (i.e., dITCZ, sITCZ, and eITCZ states). The results show that the CCW filtered variances are much higher during the sITCZ and eITCZ days for all CCWs (Figure 7). However, the eITCZ state is a rare phenomenon and is mostly active during EP El Niño years (Haffke et al. 2016).

Finally, we investigated the co-evolution of the precipitation associated with the Kelvin wave and ITCZ states. The Kelvin wave convective signal can be seen propagating from the central–west Pacific (Figure 8). The nITCZ percentage increases strongly after lag 0, while the sITCZ and dITCZ together have an overall decreasing trend, which sug-

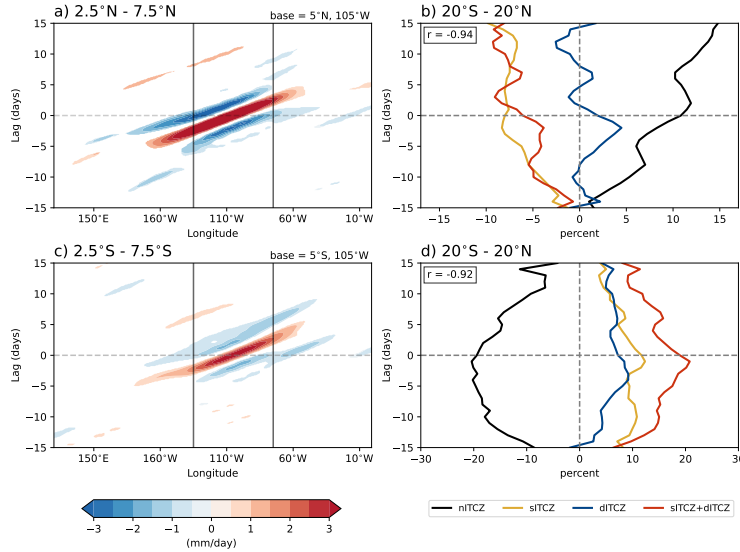


FIG. 8. Longitude–time diagram of Kelvin wave band filtered precipitation anomalies averaged between (a) $2.5^{\circ}\text{N} - 7.5^{\circ}\text{N}$ and (c) $2.5^{\circ}\text{S} - 7.5^{\circ}\text{S}$. Lag 0 corresponds to the days when the Kelvin wave-filtered precipitation anomalies are greater than one standard deviation at the NH and SH base points, shown in the top right corner. The black vertical lines enclose the ITCZ state longitude window. The anomalies shown here are 99% significant by a two-sided Student’s t test. (b) and (d) ITCZ state percent anomalies for strong Kelvin wave band activity days for the NH and SH base points, respectively. Lag 0 represents the same as in (a) and (c). The “ r ” value at the top left shows the correlation between nITCZ and sITCZ + dITCZ.

gests that increased CCW activity may facilitate the more frequent nITCZ activity. However, at the SH base point, we show that the sITCZ and dITCZ (combined) percentage increase and nITCZ percentage decrease are largest at lag 0, suggesting CCWs may excite the sITCZ or dITCZ state activity or sITCZs/dITCZs can excite CCWs in the SH.

In this study, we document that although precipitation activity is present in the NH throughout the year, variability in the precipitation is high in a fractional sense during boreal spring, and CCWs strongly influence precipitation, especially in the SH. However, further investigation of the detailed mechanisms is needed to understand the interactions between the background state, the ITCZ state, and CCW activity over the EP during boreal spring when the SH ITCZ is present. Given that earth system models struggle to capture the correct seasonality, structure, and life cycle of both CCWs and the ITCZ, future work will involve identifying CCW-ITCZ relationships in earth system models and determining which, if any, earth system models faithfully reproduce the observed CCW and ITCZ variability in the EP.

Acknowledgments. We would like to acknowledge insightful conversations with Gudrun Magnúsdóttir. We thank Carl Schreck for his methodology for calculating the percent variances of CCWs. Comments from George Kiladis and two anonymous reviewers helped improve the quality of the final manuscript. Financial support comes from NSF Grant AGS-1953944 and AGS-2303225.

REFERENCES

- Adam, O., T. Schneider, F. Brient, and T. Bischoff, 2016: Relation of the double-itcz bias to the atmospheric energy budget in climate models. *Geophys. Res. Lett.*, **43** (14), 7670–7677, doi:https://doi.org/10.1002/2016GL069465.
- Blandford, R., 1966: Mixed gravity-rossby waves in the ocean. *Deep Sea Research and Oceanographic Abstracts*, **13** (5), 941–961, doi:https://doi.org/10.1016/0011-7471(76)90912-8, URL <https://www.sciencedirect.com/science/article/pii/0011747176909128>.
- Dias, J., and G. N. Kiladis, 2014: Influence

- of the basic state zonal flow on convectively coupled equatorial waves. *Geophysical Research Letters*, **41** (19), 6904–6913, doi:<https://doi.org/10.1002/2014GL061476>, URL <https://agupubs.onlinelibrary.wiley.com/doi/abs/10.1002/2014GL061476>.
- Duffy, M. L., P. A. O’Gorman, and L. E. Back, 2020: Importance of laplacian of low-level warming for the response of precipitation to climate change over tropical oceans. *Journal of Climate*, **33** (10), 4403–4417.
- Gill, A. E., 1980: Some simple solutions for heat-induced tropical circulation. *Quarterly Journal of the Royal Meteorological Society*, **106** (449), 447–462, doi:<https://doi.org/10.1002/qj.49710644905>, URL <https://rmets.onlinelibrary.wiley.com/doi/abs/10.1002/qj.49710644905>.
- Gonzalez, A. O., I. Ganguly, M. C. McGraw, and J. G. Larson, 2022: Rapid dynamical evolution of itcz events over the east pacific. *Journal of Climate*, **35** (4), 1197 – 1213, doi:<https://doi.org/10.1175/JCLI-D-21-0216.1>, URL <https://journals.ametsoc.org/view/journals/clim/35/4/JCLI-D-21-0216.1.xml>.
- Gu, G., R. F. Adler, and A. H. Sobel, 2005: The eastern pacific itcz during the boreal spring. *Journal of the Atmospheric Sciences*, **62** (4), 1157 – 1174, doi:<https://doi.org/10.1175/JAS3402.1>, URL <https://journals.ametsoc.org/view/journals/atsc/62/4/jas3402.1.xml>.
- Guo, Y., D. E. Waliser, and X. Jiang, 2015: A systematic relationship between the representations of convectively coupled equatorial wave activity and the madden–julian oscillation in climate model simulations. *Journal of Climate*, **28** (5), 1881 – 1904, doi:[10.1175/JCLI-D-14-00485.1](https://doi.org/10.1175/JCLI-D-14-00485.1), URL <https://journals.ametsoc.org/view/journals/clim/28/5/jcli-d-14-00485.1.xml>.
- Haffke, C., G. Magnusdottir, D. Henke, P. Smyth, and Y. Peings, 2016: Daily states of the march–april east pacific itcz in three decades of high-resolution satellite data. *Journal of Climate*, **29** (8), 2981 – 2995, doi:<https://doi.org/10.1175/JCLI-D-15-0224.1>, URL <https://journals.ametsoc.org/view/journals/clim/29/8/jcli-d-15-0224.1.xml>.
- Henke, D., P. Smyth, C. Haffke, and G. Magnusdottir, 2012: Automated analysis of the temporal behavior of the double intertropical convergence zone over the east pacific. *Remote Sensing of Environment*, **123**, 418–433, doi:<https://doi.org/10.1016/j.rse.2012.03.022>, URL <https://www.sciencedirect.com/science/article/pii/S0034425712001411>.
- Hersbach, H., and Coauthors, 2020: The era5 global reanalysis. *Quarterly Journal of the Royal Meteorological Society*, **146** (730), 1999–2049, doi:<https://doi.org/10.1002/qj.3803>, URL <https://rmets.onlinelibrary.wiley.com/doi/abs/10.1002/qj.3803>, <https://rmets.onlinelibrary.wiley.com/doi/pdf/10.1002/qj.3803>.
- Huaman, L., C. Schumacher, and G. N. Kiladis, 2020: Eastward-propagating disturbances in the tropical pacific. *Monthly Weather Review*, **148** (9), 3713 – 3728, doi:<https://doi.org/10.1175/MWR-D-20-0029.1>, URL <https://journals.ametsoc.org/view/journals/mwre/148/9/mwrD200029.xml>.
- Huaman, L., and K. Takahashi, 2016: The vertical structure of the eastern pacific itczs and associated circulation using the trmm precipitation radar and in situ data. *Geophysical Research Letters*, **43** (15), 8230–8239, doi:<https://doi.org/10.1002/2016GL068835>, URL <https://agupubs.onlinelibrary.wiley.com/doi/abs/10.1002/2016GL068835>, <https://agupubs.onlinelibrary.wiley.com/doi/pdf/10.1002/2016GL068835>.
- Hubert, L. F., A. F. Krueger, and J. S. Winston, 1969: The double intertropical convergence zone—fact or fiction? *Journal of Atmospheric Sciences*, **26** (4), 771 – 773, doi:[https://doi.org/10.1175/1520-0469\(1969\)026<0771:TDICZF>2.0.CO;2](https://doi.org/10.1175/1520-0469(1969)026<0771:TDICZF>2.0.CO;2), URL https://journals.ametsoc.org/view/journals/atsc/26/4/1520-0469_1969_026_0771_tdiczf_2_0_co_2.xml.
- Huffman, G. J., D. T. Bolvin, D. Braithwaite, K. Hsu, R. Joyce, P. Xie, and S.-H. Yoo, 2015: Nasa global precipitation measurement (gpm) integrated multi-satellite retrievals for gpm (imerg). *Algorithm Theoretical Basis Document (ATBD) Version*, **4** (26).
- Hung, M.-P., J.-L. Lin, W. Wang, D. Kim, T. Shinoda, and S. J. Weaver, 2013: Mjo and convectively coupled equatorial waves simulated by cmip5 climate models. *Journal of Climate*, **26** (17), 6185 – 6214, doi:[10.1175/JCLI-D-12-00541.1](https://doi.org/10.1175/JCLI-D-12-00541.1), URL <https://journals.ametsoc.org/view/journals/clim/26/17/jcli-d-12-00541.1.xml>.
- Hwang, Y.-T., and D. M. W. Frierson, 2013: Link between the double-intertropical conver-

- gence zone problem and cloud biases over the southern ocean. *Proceedings of the National Academy of Sciences*, **110** (13), 4935–4940, doi:10.1073/pnas.1213302110, URL <https://www.pnas.org/doi/abs/10.1073/pnas.1213302110>, <https://www.pnas.org/doi/pdf/10.1073/pnas.1213302110>.
- Judt, F., and R. Rios-Berrios, 2021: Resolved convection improves the representation of equatorial waves and tropical rainfall variability in a global nonhydrostatic model. *Geophysical Research Letters*, **48** (14), e2021GL093265, doi:<https://doi.org/10.1029/2021GL093265>, URL <https://agupubs.onlinelibrary.wiley.com/doi/abs/10.1029/2021GL093265>.
- Kiladis, G. N., M. C. Wheeler, P. T. Haertel, K. H. Straub, and P. E. Roundy, 2009: Convectively coupled equatorial waves. *Reviews of Geophysics*, **47** (2), doi:<https://doi.org/10.1029/2008RG000266>, URL <https://agupubs.onlinelibrary.wiley.com/doi/abs/10.1029/2008RG000266>, <https://agupubs.onlinelibrary.wiley.com/doi/pdf/10.1029/2008RG000266>.
- Lin, J.-L., 2007: The double-ITCZ problem in IPCC AR4 coupled GCMs: Ocean–atmosphere feedback analysis. *Journal of Climate*, **20** (18), 4497 – 4525, doi:<https://doi.org/10.1175/JCLI4272.1>, URL <https://journals.ametsoc.org/view/journals/clim/20/18/jcli4272.1.xml>.
- Lin, J.-L., and Coauthors, 2006: Tropical intraseasonal variability in 14 IPCC AR4 climate models. part i: Convective signals. *Journal of Climate*, **19** (12), 2665 – 2690, doi:<https://doi.org/10.1175/JCLI3735.1>, URL <https://journals.ametsoc.org/view/journals/clim/19/12/jcli3735.1.xml>.
- Madden, R. A., and P. R. Julian, 1971: Detection of a 40–50 day oscillation in the zonal wind in the tropical Pacific. *Journal of Atmospheric Sciences*, **28** (5), 702 – 708, doi:10.1175/1520-0469(1971)028<0702:DOADOI>2.0.CO;2, URL https://journals.ametsoc.org/view/journals/atsc/28/5/1520-0469_1971_028_0702_doadoi_2_0_co_2.xml.
- Madden, R. A., and P. R. Julian, 1972: Description of global-scale circulation cells in the tropics with a 40–50 day period. *Journal of Atmospheric Sciences*, **29** (6), 1109 – 1123, doi:10.1175/1520-0469(1972)029<1109:DOGSCC>2.0.CO;2, URL https://journals.ametsoc.org/view/journals/atsc/29/6/1520-0469_1972_029_1109_dogsc_2_0_co_2.xml.
- Mapes, B. E., T. T. Warner, and M. Xu, 2003: Diurnal patterns of rainfall in northwestern South America. part iii: Diurnal gravity waves and nocturnal convection offshore. *Monthly Weather Review*, **131** (5), 830 – 844, doi:10.1175/1520-0493(2003)131<0830:DPORIN>2.0.CO;2, URL https://journals.ametsoc.org/view/journals/mwre/131/5/1520-0493_2003_131_0830_dpoin_2.0.co_2.xml.
- Matsuno, T., 1966: Quasi-geostrophic motions in the equatorial area. *Journal of the Meteorological Society of Japan. Ser. II*, **44** (1), 25–43, doi:10.2151/jmsj1965.44.1_25.
- Mayta, V. C., G. N. Kiladis, J. Dias, P. L. S. Dias, and M. Gehne, 2021: Convectively coupled Kelvin waves over tropical South America. *Journal of Climate*, **34** (16), 6531 – 6547, doi:<https://doi.org/10.1175/JCLI-D-20-0662.1>, URL <https://journals.ametsoc.org/view/journals/clim/34/16/JCLI-D-20-0662.1.xml>.
- Mechoso, C., and Coauthors, 1995: The seasonal cycle over the tropical Pacific in coupled ocean–atmosphere general circulation models. *Monthly Weather Review*, **123** (9), 2825 – 2838, doi:[https://doi.org/10.1175/1520-0493\(1995\)123<2825:TSCOTT>2.0.CO;2](https://doi.org/10.1175/1520-0493(1995)123<2825:TSCOTT>2.0.CO;2), URL https://journals.ametsoc.org/view/journals/mwre/123/9/1520-0493_1995_123_2825_tscott_2_0_co_2.xml.
- Roundy, P. E., 2020: Interpretation of the spectrum of eastward-moving tropical convective anomalies. *Quarterly Journal of the Royal Meteorological Society*, **146** (727), 795–806, doi:<https://doi.org/10.1002/qj.3709>, URL <https://rmets.onlinelibrary.wiley.com/doi/abs/10.1002/qj.3709>, <https://rmets.onlinelibrary.wiley.com/doi/pdf/10.1002/qj.3709>.
- Roundy, P. E., and W. M. Frank, 2004: A climatology of waves in the equatorial region. *Journal of the Atmospheric Sciences*, **61** (17), 2105 – 2132, doi:[https://doi.org/10.1175/1520-0469\(2004\)061<2105:ACOWIT>2.0.CO;2](https://doi.org/10.1175/1520-0469(2004)061<2105:ACOWIT>2.0.CO;2), URL https://journals.ametsoc.org/view/journals/atsc/61/17/1520-0469_2004_061_2105_acowit_2.0.co_2.xml.
- Schreck, C. J., L. Shi, J. P. Kossin, and J. J. Bates, 2013: Identifying the MJO, equatorial waves, and their impacts using 32 years of HIRS upper-tropospheric water vapor. *Journal of Climate*, **26** (4), 1418 – 1431, doi:<https://doi.org/10.1175/JCLI-D-12-00034.1>, URL <https://journals.ametsoc.org/view/journals/clim/26/4/jcli-d-12-00034.1.xml>.
- Si, W., H. Liu, X. Zhang, and M. Zhang,

- 2021: Double intertropical convergence zones in coupled ocean-atmosphere models: Progress in cmip6. *Geophysical Research Letters*, **48** (23), e2021GL094779, doi:<https://doi.org/10.1029/2021GL094779>, URL <https://agupubs.onlinelibrary.wiley.com/doi/abs/10.1029/2021GL094779>, e2021GL094779 2021GL094779, <https://agupubs.onlinelibrary.wiley.com/doi/pdf/10.1029/2021GL094779>.
- Song, X., and G. J. Zhang, 2019: Culprit of the Eastern Pacific Double-ITCZ Bias in the NCAR CESM1.2. *J. Climate*, **32** (19), 6349–6364, doi:10.1175/JCLI-D-18-0580.1.
- Straub, K. H., and G. N. Kiladis, 2002: Observations of a convectively coupled kelvin wave in the eastern pacific itcz. *Journal of the Atmospheric Sciences*, **59** (1), 30 – 53, doi:[https://doi.org/10.1175/1520-0469\(2002\)059<0030:OOACCK>2.0.CO;2](https://doi.org/10.1175/1520-0469(2002)059<0030:OOACCK>2.0.CO;2), URL https://journals.ametsoc.org/view/journals/atsc/59/1/1520-0469_2002_059_0030_ooacck_2.0.co_2.xml.
- Straub, K. H., and G. N. Kiladis, 2003: Extratropical forcing of convectively coupled kelvin waves during austral winter. *Journal of the Atmospheric Sciences*, **60** (3), 526 – 543, doi:[https://doi.org/10.1175/1520-0469\(2003\)060<0526:EFOCCK>2.0.CO;2](https://doi.org/10.1175/1520-0469(2003)060<0526:EFOCCK>2.0.CO;2), URL https://journals.ametsoc.org/view/journals/atsc/60/3/1520-0469_2003_060_0526_efocck_2.0.co_2.xml.
- Takayabu, Y. N., and T. Nitta, 1993: 3-5 day-period disturbances coupled with convection over the tropical pacific ocean. *Journal of the Meteorological Society of Japan. Ser. II*, **71** (2), 221–246, doi:10.2151/jmsj1965.71.2_221.
- Wang, C.-C., W.-L. Lee, Y.-L. Chen, and H.-H. Hsu, 2015: Processes Leading to Double Intertropical Convergence Zone Bias in CESM1/CAM5. *J. Climate*, **28** (7), 2900–2915, doi:10.1175/JCLI-D-14-00622.1.
- Wheeler, M., and G. N. Kiladis, 1999: Convectively coupled equatorial waves: Analysis of clouds and temperature in the wavenumber–frequency domain. *Journal of the Atmospheric Sciences*, **56** (3), 374 – 399, doi:[https://doi.org/10.1175/1520-0469\(1999\)056<0374:CCEWAO>2.0.CO;2](https://doi.org/10.1175/1520-0469(1999)056<0374:CCEWAO>2.0.CO;2), URL https://journals.ametsoc.org/view/journals/atsc/56/3/1520-0469_1999_056_0374_ccewao_2.0.co_2.xml.
- Wheeler, M., G. N. Kiladis, and P. J. Webster, 2000: Large-scale dynamical fields associated with convectively coupled equatorial waves. *Journal of the Atmospheric Sciences*, **57** (5), 613 – 640, doi:[https://doi.org/10.1175/1520-0469\(2000\)057<0613:LSDFAW>2.0.CO;2](https://doi.org/10.1175/1520-0469(2000)057<0613:LSDFAW>2.0.CO;2), URL https://journals.ametsoc.org/view/journals/atsc/57/5/1520-0469_2000_057_0613_lsdhaw_2.0.co_2.xml.
- Wilks, D. S., 2016: “the stippling shows statistically significant grid points”: How research results are routinely overstated and overinterpreted, and what to do about it. *Bulletin of the American Meteorological Society*, **97** (12), 2263 – 2273, doi:<https://doi.org/10.1175/BAMS-D-15-00267.1>, URL <https://journals.ametsoc.org/view/journals/bams/97/12/bams-d-15-00267.1.xml>.
- Yang, W., and G. Magnusdottir, 2016: Interannual signature in daily itcz states in the east pacific in boreal spring. *Journal of Climate*, **29** (22), 8013 – 8025, doi:<https://doi.org/10.1175/JCLI-D-16-0395.1>, URL <https://journals.ametsoc.org/view/journals/clim/29/22/jcli-d-16-0395.1.xml>.
- Zhang, C., 2001: Double ITCZs. *J. Geophys. Res.*, **106**, 11 785–11 792, doi:10.1029/2001JD900046.
- Zhang, X., H. Liu, and M. Zhang, 2015: Double itcz in coupled ocean-atmosphere models: From cmip3 to cmip5. *Geophysical Research Letters*, **42** (20), 8651–8659, doi:<https://doi.org/10.1002/2015GL065973>, URL <https://agupubs.onlinelibrary.wiley.com/doi/abs/10.1002/2015GL065973>, <https://agupubs.onlinelibrary.wiley.com/doi/pdf/10.1002/2015GL065973>.